Properties of the CsI(Tl) detector elements of the CALIFA detector

A. Knyazev [a], J. Park [a], P. Golubev [a], J. Cederkäll [a,*], H. Alvarez-Pol [b], P. Cabanelas [b], E. Casarejos [d], L. Causeret [a], D. Cortina-Gil [b], P. Díaz Fernández [c], M. Feijoo [b], D. Galaviz [e], E. Galiana [e], R. Gernhäuser [f], A.-L. Hartig [g], A. Heinz [c], B. Heiss [f], A. Ignatov [g], H. Johansson [c], P. Klenze [f], T. Kröll [g], T. Nilsson [c], A. Perea [h], H.-B. Rhee [g], O. Tengblad [h], P. Teubig [e]

[a] *Department of Physics, Lund University, SE-221 00 Lund, Sweden*
[b] *Dpt. de Física de Partículas, Universidade de Santiago de Compostela, E-15782 Santiago de Compostela, Spain*
[c] *Department of Physics, Chalmers University of Technology, S-41296 Gothenburg, Sweden*
[d] *Universidade de Vigo, E-36310 Vigo, Spain*
[e] *Laboratory for Instrumentation and Experimental Particle Physics, 1649-003 Lisbon, Portugal*
[f] *Physik Department, Technische Universität München, 85748 Garching, Germany*
[g] *Institut für Kernphysik, Technische Universität Darmstadt, D-64289 Darmstadt, Germany*
[h] *Instituto de Estructura de la Materia, CSIC, E-28006 Madrid, Spain*

ARTICLE INFO

ABSTRACT

In the R³B experiment at FAIR, charged particles with energies up to 600 MeV and forward boosted γ-rays with energies up to 20 MeV need to be detected in scattering experiments. Calorimeters for nuclear physics experiments of this kind, using relativistic radioactive ion beams, require high energy resolution and high efficiency for simultaneous detection of strongly Doppler shifted γ-rays and high-energy charged particles. A calorimeter design that can meet these requirements, using CsI(Tl) scintillators, results in detector elements that may exhibit light output variations with crystal depth, which can limit the attainable resolution. In this paper we present results from a systematic study of 478 detector modules of CALIFA, the R³B calorimeter, in order to determine and minimize such variations. To facilitate further systematic studies we also present results for the total absorption length of the scintillation light, using spectrophotometry, light crosstalk between adjacent detector modules, and surface topography of the CsI(Tl) crystals from atomic force microscopy.

1. Introduction

The Reactions with Relativistic Radioactive Beams (R³B) experiment [1] at the Facility for Antiproton and Ion Research (FAIR) [2] is dedicated to kinematically complete measurements of reactions of radioactive atomic nuclei with energies up to 1 GeV/u. The physics cases include investigations of nuclear structure far from stability, reactions of astrophysical interest and studies of isospin-asymmetric nuclear matter. The CALorimeter for In-Flight detection of γ-rays and light charged pArticles (CALIFA) [3], positioned around the R³B target, is the calorimeter of the experiment, and will be part of the key instrumentation for many of these studies.

Products emitted from reactions studied at R³B will, due to the relativistic velocities of the incoming beam, experience significant forward boosts. While the physics cases under study require the detection of

high energy charged particles they also require simultaneous detection of γ-rays with energies between 100 keV and 20 MeV with an energy resolution of ∼7% or better at ∼1 MeV. Consequently, the detector should facilitate efficient Doppler correction and provide sufficient stopping power for detection of both charged particles and γ-rays at high energy. This leads to a highly segmented detector design with long tapered detector modules [4].

To meet the design criteria CALIFA is divided into two main sections: a Barrel section that covers polar angles between 43° and 140°, and a forward endcap between 7° and 43°. The Barrel section comprises 1952 CsI(Tl) crystals, with lengths from 12 cm to 22 cm, of which 478 crystals with lengths of 17 cm, 18 cm and 22 cm have been investigated in this study. The forward endcap is divided into two subsections: the intrinsic Phoswich (iPhos) [5] and the CALIFA Endcap Phoswich Array (CEPA) [6] which covers the most forward angles between 7° and 20°. The iPhos contains 480 CsI(Tl) crystals of 22 cm length, while
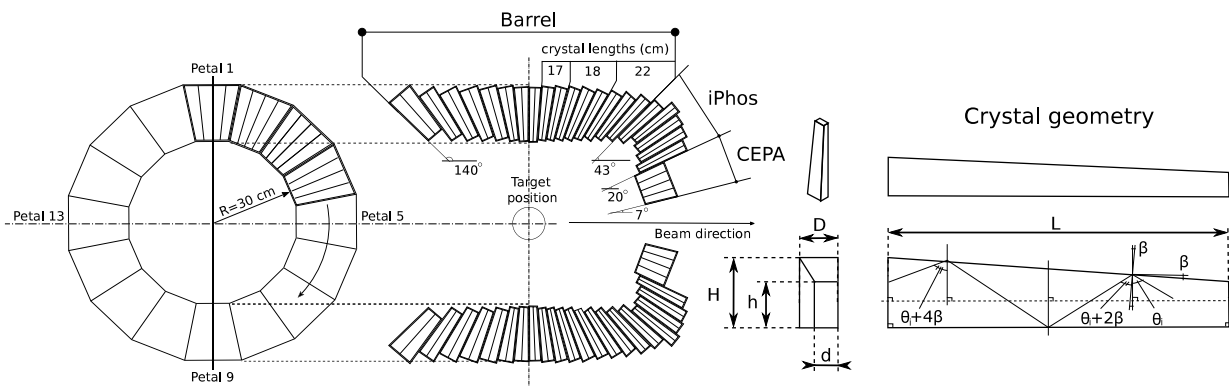

Fig. 1. Overview of the CALIFA detector and its three sections: the Barrel, iPhos [5] and CEPA [6]. The geometry is determined by the requirement to stop high-energy charged particles while maintaining a high-granularity for Doppler correction of γ-rays emitted from the reactions with the incoming relativistic beam [4]. The Barrel contains a total of 1952 CsI(Tl) detector elements of which a subset was studied as to resolution and light output uniformity in this work. The geometry of the respective crystals is given to the right in the figure with an illustration of the focussing effect discussed in the text. Reflection on the tapered side of the crystal, defined by the tapering angle β and the incoming angle θ_i, leads to a change in reflection angle along the path. For further details see the text. For crystal dimensions see Table 1.

Table 1
Crystal types, sizes and numbers of crystals tested in this work. Distances as defined in Fig. 1. The two geometries per row constitute mirror images. The 1113/1114 geometries are a minor variation on 1101/1102 with a slightly tilted upper surface. For these crystals the height at the midpoint is given for a total difference of ca 1 mm between the two sides. All distances are given in mm.

Geometry	Nr	L	D	d	H	h
1101/1102	89	220	25	15	45	29
1103/1104	179	180	23	15	45	29
1105/1106	120	170	23	15	45	29
1113/1114	90	220	25	15	47	30

the CEPA is a $LaBr_3/LaCl_3$ phoswich array with 96 detector elements. Fig. 1 and Table 1 give an overview of the geometry of the detector system and the Barrel detector modules treated in this work. The detector modules consist of CsI(Tl) crystals produced using the liquid Czochralski method,[1] wrapped in ESR foil,[2] with an array of two Si APDs, in a single ceramic package,[3] coupled to the larger end surface of the crystals using optical resin.[4]

In scintillation crystals of the current geometry the combination of light absorption and focussing can result in different amounts of scintillation light being read out at the end surface of the crystal for events occurring at different crystal depths, even if the amount of deposited energy, and thus the average number of scintillation photons created, is the same. Such a non-uniform response will oppose the resolution requirement for γ-ray detection and be particularly detrimental for cases where signal add back between crystals is performed.

The current work is motivated by the need to properly understand the influence of such effects on the CALIFA detection performance. The crystals under investigation have been subject to a state-of-the-art lapping procedure on the four lateral sides before delivery in order to improve the uniformity of light output. This technique is well established and has been discussed in the literature earlier [7–9]. A general discussion of how the surface structure of a scintillator can influence the light output is also given in the textbook by Birks [10].

One aim of this study is to see to what extent the lapping procedure has resulted in a random correlation between light output non-uniformity and resolution for the large set of crystals investigated here. On the other hand, if a correlation remains between these two variables, it is interesting to determine what the best attainable resolution is for the system as a whole.

To briefly reiterate the discussion given in previous work, the origin of light output non-uniformity in polished long tapered scintillator crystals comes from two effects, scintillation light absorption and focussing [7–9]. As expected, the first effect, absorption, leads to less light reaching the readout sensor for scintillation events occurring further
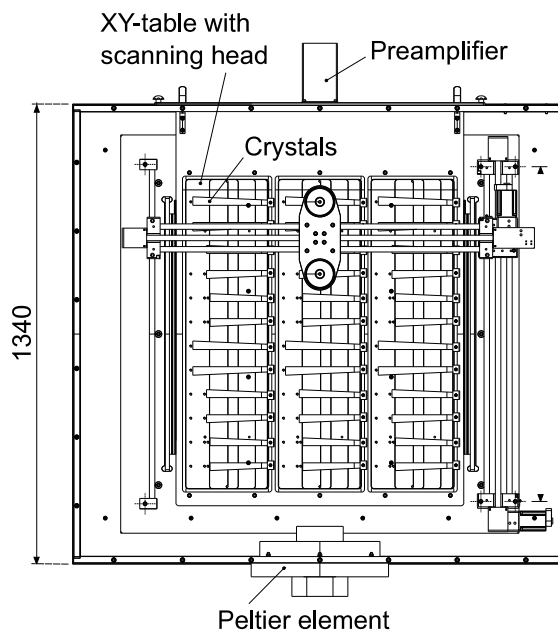

Fig. 2. Top view of the scanning table used for the light output measurements. The setup is enclosed in a thermally insulated and light tight container. A set of 32 crystals can be loaded for consecutive scanning. A typical measurement series uses ten measurement points per crystal and completes, on average, 5 detector modules per hour. The Peltier element mounted on the side port facilities measurements of the detector response at different temperatures. The size of the setup is indicated by the measure on the left hand side (in mm).

away from the sensor. How quickly the intensity falls off with increasing distance depends on the attenuation length in the crystal. The second effect, focussing, which is specific to tapered crystals, works in the opposite way, and leads to a relative increase in the amount of light that reaches the readout sensor as the distance between the scintillation event and the sensor increases. This effect has a simple explanation as well. Light that undergoes specular reflections on the surface of a polished tapered crystal will, for each reflection at incoming angle θ_i, with respect to the normal relative to the central axis of the crystal, reflect into an angle $\theta_i + 2\beta$, where β is the tapering angle [7–9]. This gradual increase of the outgoing reflection angle allows light emitted into a solid angle larger than the one given by the line of sight, from the point of emission to the sensor, to hit the sensor surface at angles close to 90°, which leads to a relative increase in detected intensity with
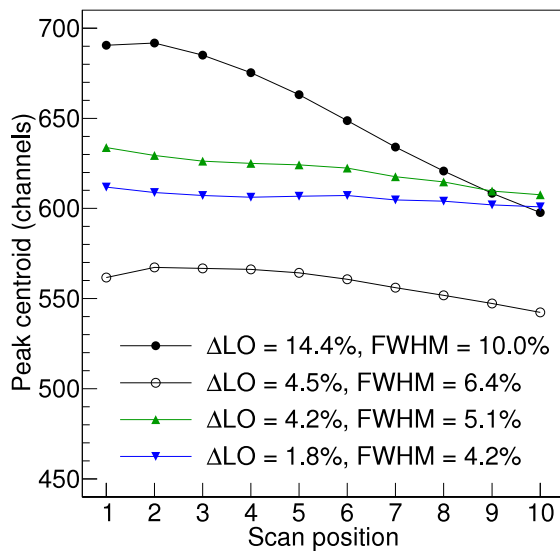
Fig. 3. Example results from light output non-uniformity measurements on three crystals. The first scan position (1) is furthest away from the APD and the last one (10) is closest. The filled black circles show the light output non-uniformity for a completely polished test crystal. The focussing effect dominates and the ΔLO and FWHM are 14.4% and 10.0%, respectively. After lapping ΔLO improves to 4.5% and the FWHM to 6.4% (open circles) at the same time as the total light output becomes smaller. The results for two production run crystals are shown as well (green and blue triangles). These have ΔLOs of 4.2% and 1.8% respectively, with the corresponding FWHMs of 5.1% and 4.2%. The FWHM was measured at 1275 keV and the light output non-uniformity at 662 keV. For further details see the text. (For interpretation of the references to colour in this figure legend, the reader is referred to the web version of this article.)

distance. This effect is reproduced in simulations [8,9]. The geometry relevant for the focussing effect in this work is clarified in Fig. 1.

One way to reduce the light output non-uniformity of a polished crystal is to rough the surface by lapping it. The highly ordered polished surface will then be divided into microfacets whose normals will point in random directions with respect to the normal of the macroscopic surface. These microfacets will in turn introduce a random distribution in the path lengths for scintillation light that is reflected at the boundaries, which will reduce the differences in detected intensity as a function of distance. This effect is also reproduced in the simulations presented in Refs. [8,9]. Precise simulation results, however, require knowledge of the attenuation length and surface topography for the specific case.

In the following we present results for detector resolution and its correlation to total light output, light output non-uniformity and efficiency for a set of 478 detector modules. The influence on the energy resolution from noise and temperature variations is also quantified. In addition, results from measurements of the mean free path of scintillation light in CsI(Tl), light crosstalk and signal add back between detector modules were investigated. Surface topography, of importance for light transport simulations in scintillator crystals, is also discussed in relation to an atomic force microscopy measurement.

2. Light output and resolution

In addition to intrinsic material properties, the total absorption length for large crystals depends on material imperfections that can arise in the manufacturing process or as a result of radiation damage [11]. The focussing effect in turn depends on crystal geometry and surface topography since the amount of scintillation light reflected towards and into the read-out sensor, depends on the angles of reflection along the propagation path [9]. It is therefore necessary, as part of a characterization study, to measure the absorption over the full emission spectrum and to measure the crystals surface topography if one aims to properly understand the detector performance, e.g. from light collection simulations.

In addition to these two effects uneven doping can also lead to light output variations, particularly in large crystals. However, it has been shown that the maximum light output for CsI(Tl) can be expected at a Tl-doping level of ~0.1% and that variations in doping around this value should have limited influence on the light output [12]. The crystals for CALIFA are manufactured with the criterion of having a Tl-doping level between 0.08 and 0.12% which should lead to a variation in total light output of ~5%. One way to verify whether the doping concentration is as stipulated is to perform Proton Induced X-ray Emission measurements on the crystals [13]. Such studies are underway as part of the current project and are planned to be presented in a later publication.

2.1. Measurement procedure

Due to the large number of crystals in CALIFA, it was necessary to automate the crystal performance measurements. For this reason a testing station was constructed to examine crystal light output and the attainable energy resolution for the detector system. The testing station consists of a light-, thermo- and RF-insulated enclosed volume (see Fig. 2) with a scanning head connected to two stepping motors that provide two-dimensional motion in the plane. The positioning of the scanning head, controlled via a dedicated software, is done with a stepper motor-driven linear stage with a spatial resolution of 12 μm.[5] The scanning head has two ports that allow for simultaneous use of two γ-ray sources that can be collimated down to 0.01 sr. The crystals are loaded in three main cells that together have a total of 36 positions. Up to 32 crystals can be tested in one batch using the readout chain.

A Peltier element,[6] regulated via a proportional, integral and derivative control loop connected to a temperature sensor with an accuracy of ≲0.1 K, is also connected to a side port. The Peltier element makes it possible to measure the gain dependence on temperature as well as the effect of the preamplifier temperature compensation algorithm and the thermal stability of the optical contact between the scintillator and the APD.

Since CsI(Tl) is weakly hygroscopic [14], the crystals are kept in a desiccator cabinet,[7] providing an atmosphere with relative humidity ≲1% between tests.

The electronic read-out chain of the setup is identical to the one used in the R^{3}B experiment [15] and includes a preamplifier,[8] a fast sampling ADC,[9] and the MBS data acquisition system [16,17]. Special care was taken to ensure that potential noise from external sources other than the readout chain was eliminated during the measurements.

For the light output non-uniformity measurements collimated ^{137}Cs [18] sources (E_γ = 662 keV), located 90 mm above the samples, and illuminating a circular area with radius 7 mm on the crystal surface, were used. The energy resolution and photopeak position of 10 equidistant points along the crystal were measured for each crystal (see Fig. 3). The figure of merit used to quantify the non-uniformity of the light output in this work is defined as:

$$\Delta\text{LO} = \frac{C_{\max} - C_{\min}}{\frac{1}{N}\sum_{i=1}^{N} C_i} \times 100\%, \tag{1}$$

where N is the number of measurement points and $C_{\max}$ and $C_{\min}$ are the maximum and minimum centroid positions of Gaussians fitted to the photopeaks of the measurement points of each crystal, respectively. It is important to note that a large non-uniformity naturally leads to a lower resolution since the total response of a crystal will consist of the summed response from all its parts. In the following we use correlations to see which effect dominates variations in resolution.
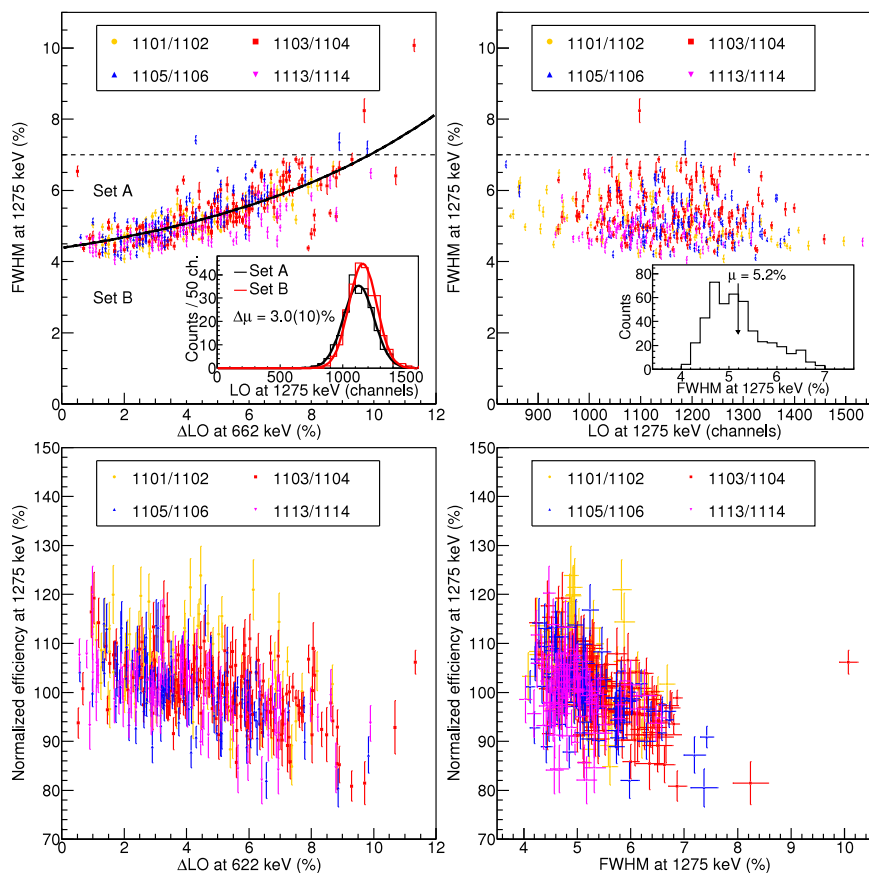
Fig. 4. Upper left: the energy resolution, FWHM, at 1275 keV versus light output non-uniformity, ΔLO, at 662 keV for the 478 crystals investigated. The markers indicate different crystal geometries. The dashed line at FWHM = 7% corresponds to the final acceptance criterion at this γ-ray energy. The solid line shows a fit to an exponential used to divide the crystals into two sets. The inset shows the light output of crystals in set A (lower resolution) compared to that of crystals in set B (higher resolution). Upper right: the FWHM versus light output, LO, for the same set, measured at 1275 keV. The inset shows the projection on the FWHM axis. Lower left: Correlation between normalized efficiency, EFF, at 1275 keV and ΔLO, at 662 keV, as above. Lower right: EFF versus FWHM correlation measured at 1275 keV. See text for details.

As an illustration Fig. 3 shows a comparison between the non-uniformity for a polished crystal, and for the same crystal lapped on all four lateral sides. The test case shows an improvement from a non-uniformity of 14.4% to 4.5% after lapping with a corresponding improvement in resolution from 10.0% to 6.4%. The total light output is affected, as expected in view of the discussion above, but the overall effect is still an improvement of the resolution. Two examples from the production are also given in Fig. 3, with light output non-uniformities of 1.8% and 4.2%, respectively, and corresponding resolutions of 4.2% and 5.2%. The variations observed in ΔLO between crystals depend critically on the attenuation length and surface treatment, due to the combined effect of the absorption and focussing effects as discussed above, and potentially on variations in doping level. It is thus expected that ΔLO varies over the detector sample.

The energy resolution of the detector modules was measured with an uncollimated ^{22}Na ($E_\gamma = 1275$ keV) source [19], positioned above the centre of the long side of each crystal. Based on the demand from the physics program mentioned above, a worst case resolution of 7% was used as an acceptance criterion for individual crystals. As is shown below, this condition led to an average resolution well below this limit for the total set. The relative efficiency of the crystals was extracted by comparing the number of photopeak events, registered for the 1275 keV γ-ray from the ^{22}Na source, in the resolution measurements. The purpose of these measurements was to provide an additional method to ensure that the crystals did not have mechanical or other internal defects. All measurements were carried out with the APDs at their nominal voltages, corresponding to a gain, $M = 50$, at $\lambda = 420$ nm and $T = 25$ °C, with the preamplifier temperature compensation algorithm activated. Table 2 summarizes the results.

Table 2

The resolution (FWHM), light output non-uniformity (ΔLO), (both in percent), the light output (LO) and normalized efficiency (EFF) for the different geometries studied in this work, and their respective standard deviations. The relative efficiency and the light output are normalized to the mean of the full set. The resolution, efficiency and light output were measured at 1275 keV and light output non-uniformity at 662 keV. See text for further details.

Geometry	FWHM (%)	ΔLO (%)	LO (%)	EFF (%)
1101/1102	5.1 ± 0.6	4.0 ± 2.0	98.6 ± 12	96.7 ± 6.7
1103/1104	5.4 ± 0.6	5.0 ± 2.0	100.6 ± 9.3	98.9 ± 6.4
1105/1106	5.1 ± 0.6	3.8 ± 1.6	102.7 ± 8.2	100.3 ± 5.8
1113/1114	5.0 ± 0.5	4.1 ± 2.1	96.0 ± 8.0	102.3 ± 6.7
Total	5.2 ± 0.6	4.2 ± 2.0	100.0 ± 9.5	100.0 ± 6.6

2.2. Correlation histograms

Total light output and its variation along the crystals axes, the relative efficiency and the energy resolution were investigated for the eight geometries that cover the forward part of the Barrel. Two-dimensional correlation histograms between the resolution (FWHM), light output (LO), light output non-uniformity (ΔLO) and relative efficiency (EFF) were produced for the 478 crystals, and the correlation factor, given by the covariance between pairs of these variables, normalized by their respective standard deviations, were extracted. Results of this analysis are presented in Fig. 4 and Table 3 where the geometries (see Fig. 1 and Table 1) and the three categories of crystals, 22 cm, 18 cm and 17 cm long, can be identified.

A relatively strong correlation (see top left panel of Fig. 4) is observed between attained resolution and light output non-uniformity.

Similarly, it is also clear from the histogram of resolution versus light output, shown in the top right panel of Fig. 4, that there is very little correlation between those two variables in the sample. Numerically the correlation factor between total light output and resolution is also significantly weaker, at 0.21, than the correlation between light output non-uniformity and resolution, at 0.76. Consequently, the dependence of the resolution on the brightness of the crystals is masked by variations in the amount of light collected from different positions along the crystal axis. It can be noted that the distribution of the FWHMs, shown in the inset of the top right panel of Fig. 4, can be perceived to consist of a main distribution, and a distribution for a set of outliers extending up to a FWHM ∼7%. It should be pointed out that there are not any known systematic differences in the manufacturing procedures that would create two such distributions in the current set.

In order to investigate the dependence of the resolution on total light output further, one can note that the correlation in the top left panel of Fig. 4 is rather narrowly scattered around a moving FWHM mean, indicated by the black line in the figure (from a fit of an exponential to describe the overall behaviour). To see if the observed spread can be attributed to the brightness of the crystals, a cut was made above and below the moving mean, and the light output for the crystals selected in this way was projected out. The result, shown on the inset of the same panel, indicates that the crystals whose resolution is higher than the moving mean are on average slightly brighter than crystals above the mean, but the effect amounts only to a shift of $3.0 \pm 0.1\%$, which is significantly smaller than the observed spread. Further binning of the sample along the ΔLO axis confirms that the effect exists, and gets relatively more pronounced for crystals with small ΔLO, but this analysis does not generally prove that all crystals below the moving mean are brighter than those above it. It is even so that changing the sample sets A and B to select only crystals that deviate strongly from the mean reduces the effect rather than making it more pronounced. This is likely a sign that the crystals whose resolutions deviate significantly from the mean, at a given ΔLO, do so due to defects that cannot be readily identified within the available set.

The correlation factors between light output non-uniformity and efficiency, and resolution and efficiency, are approximately the same at -0.48 and -0.43, respectively (see the two lower panels in Fig. 4, and Table 3). This suggests that crystals with high light output non-uniformity have lower photopeak efficiency. This effect can be understood from the fact that a crystal with a large light output non-uniformity exhibits a photopeak that is the sum of photopeak responses spread out over a wider range of the spectrum than crystals with a small light output non-uniformity. The non-uniformity thus influences the shape of the photopeak. This is observed as an increase in the FWHM, but at the same time more events will also end up in the wings of the photopeak, or outside the photopeak area fitted in the analysis, and thus reduce the observed photopeak efficiency. This effect, originating in the light output non-uniformity, also explains the negative correlation between the observed photopeak efficiency and the resolution. As the peak becomes wider and the FWHM increases, due to higher light output non-uniformity, the total number of events in the peak will become smaller and thus lead to the observed correlation between FWHM and efficiency. As mentioned above, the light output non-uniformity is influenced by impurities and defects in the crystal, which in this way also influence the observed photopeak efficiency.

Finally, the collected statistics show that an average resolution of 5.2% at 1275 keV was obtained for the full set which provides a performance parameter that can be used in further simulations of the CALIFA detector response in future experiments. It can also be concluded that if the dependence on non-uniform light output could be eliminated, the resolution would improve to 4.4%.

The results presented here emphasize the importance of a systematic approach when minimizing the light output non-uniformity in order to optimize the resolution. The crystal sample used for this study exhibits variations in total light yield of $\pm$ 20% but still these variations do

Table 3
Correlation factor (C. F.) and covariance (Cov.) between resolution (FWHM), light output non-uniformity (ΔLO), total light output (LO), and normalized efficiency (EFF). The resolution has its strongest correlation with light output non-uniformity and a significantly weaker dependence on the total light output (see text for discussion).

| Var. 1	Var. 2	C. F.	Cov.
FWHM	ΔLO	0.76	1.1
FWHM	LO	0.21	1.6
FWHM	EFF	-0.43	-2.1
LO	EFF	-0.20	-15.0
LO	ΔLO	0.06	1.4
ΔLO	EFF	-0.48	-7.0
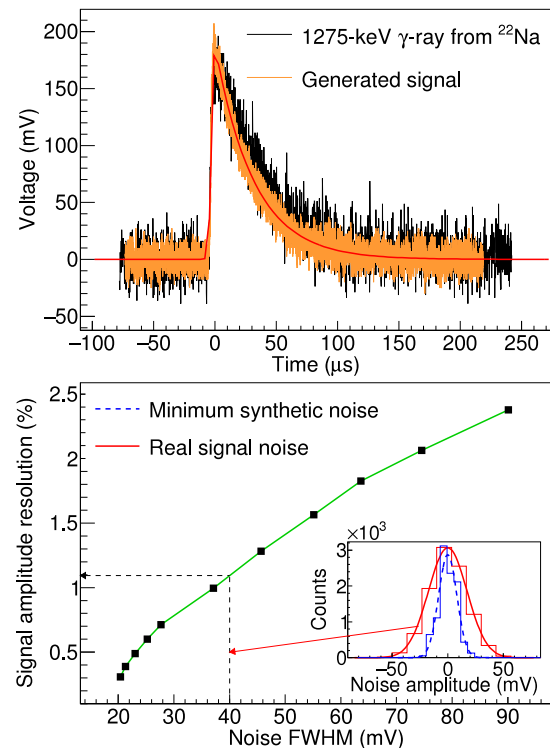
Fig. 5. Top panel: signal trace measured for the 1275 keV ^{22}Na γ-ray (black). The fitted function (red curve) was used to generate a signal of the same shape and amplitude with synthetic noise added (orange). Bottom panel: The measured resolution in per cent for the artificially generated signal as function of applied synthetic noise. The noise band for the real signal is given by the red curve in the inset and the minimum achievable noise in blue. The dashed line shows that the noise from the readout chain including the APD gives a resolution of 1.1%. The green line is to guide the eye. (For interpretation of the references to colour in this figure legend, the reader is referred to the web version of this article.)

not dominate the variations in resolution. Further improvements of the procedure used to minimize the light output non-uniformity ultimately depends, in turn, on the possibility to perform reliable simulations of the light collection process in large crystals. We discuss this further in Section 3.

2.2.1. Intrinsic resolution of the readout chain

The preamplifier used in the CALIFA readout chain gives a differential signal output that is fed into the sampling ADC, where an FPGA firmware algorithm processes the sampled signal to give energy, time and Particle ID (PID) information [5]. This makes the system rather robust against electronic noise. However, in order to separately determine the intrinsic resolution of the readout chain under realistic conditions, a dedicated measurement was carried out.
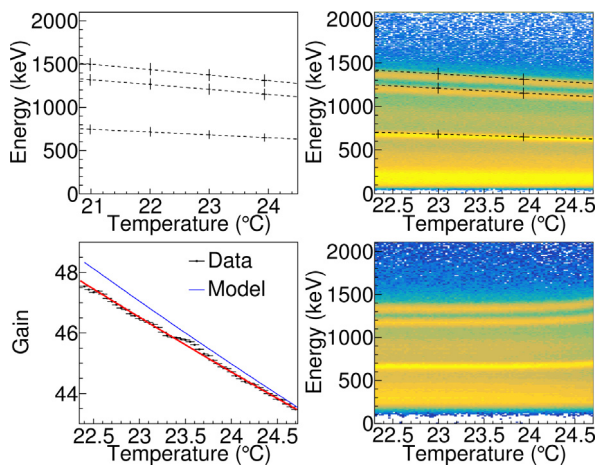
Fig. 6. Upper left panel: the signal amplitude from a detector element versus temperature, without APD temperature compensation, measured using the equilibrium approach described in the text. The measured data are represented by crosses. The dashed line shows a fit of a second order polynomial to the measurement points. Upper right panel: two-dimension histogram showing the signal amplitude from the same detector element measured while driving the temperature from ~25 °C to ~22 °C. The fitted curve from the top left panel is superimposed together with the measurement points from the equilibrium approach. Lower left panel: the gain as a function of temperature calculated from the measurement points in the upper right panel as discussed in the text [20,21]. The red curve shows an exponential fit to the data while the blue curve is the nominal curve [15,21]. Lower right panel: amplitude measurement with APD gain stabilization for temperature compensation. The ordinate for all amplitude measurements is energy calibrated at the typical ambient temperature of 23 °C. For further details see the text. (For interpretation of the references to colour in this figure legend, the reader is referred to the web version of this article.)

A typical waveform corresponding to the CsI(Tl) photopeak of the 1275 keV γ-ray from a ^{22}Na source was digitized using an oscilloscope[10] and a differential probe.[11] The registered waveform was fitted to an exponential decay curve and the fitted curve was used to generate a pulse with the same shape using a programmable function generator.[12] The pulse was fed into the sampling ADC and processed by the CALIFA data acquisition (DAQ) system.

The peak registered in the spectrum measured in this way was fitted to a Gaussian function and the resolution was determined from the FWHM of the fitted curve and the position of the centroid. The width of the noise band for this measurement was ~20 mV which can be compared to the ~40 mV noise band that was registered for the real signal when the readout system was connected to the detector module, including the APD.

Synthetic white noise, varied between 20 mV, the minimum achievable, and 90 mV was also introduced to the measurement chain to investigate the dependence of resolution on the noise level. The results are presented in Fig. 5. It was observed that the resolution varied from ~0.3% to 2.4% when the noise band was increased from 20 to 90 mV. At the typical noise level of 40 mV, measured for the real signal, the resolution is 1.1%. Consequently, assuming that the noise contribution to the overall resolution is incoherently added to the statistical fluctuation in the number of scintillation photons, the best attainable intrinsic resolution from the CsI(Tl) crystals used for CALIFA is 4.3% at 1275 keV, if the noise from the full readout chain, including the APD, is removed by quadratic subtraction.

2.3. Thermal response

The APD gain dependence on temperature and voltage is also a potential source of resolution variations when APDs are used in spectroscopy experiments [22]. The origins of these effects have been discussed in the literature [20,23,24] and depend on changes in the electron–phonon interactions with temperature, and the increase in avalanche multiplication with applied voltage. In short, within a limited temperature range, both dependencies can be considered exponential in nature, with the gain increasing with increased voltage but decreasing with increased temperature. This means that temperature gain stabilization can be accomplished by voltage variations using a linear function between the applied voltage and the measured temperature.

In order to estimate the temperature dependence of the gain for the CALIFA detector modules, the energy spectrum was measured for a ^{60}Co and a ^{137}Cs source in two thermal regimes, using an equilibrium and a non-equilibrium approach. Data collection was done with the CALIFA DAQ-system described above.

In the equilibrium regime the temperature in the measurement volume was regulated to a given set value and left at that temperature for ~900 s to achieve thermal stability before the energy spectrum was collected for ~480 s. These measurements were carried out while changing the temperature to cover an interval from ~21°C to ~26°C. The result, with the position of the photopeaks within the temperature range of interest, is given by the five markers in the upper left panel of Fig. 6. The dashed line in the same figure is from a fit of a second order polynomial to the measurement points to show the trend.

In the second measurement series the temperature was first driven above 25°C after which it is was forced to ~22°C while the spectrum was continuously recorded. The total time for the measurement was ~2300 s. The result is given by the two-dimensional histogram in the top right panel of Fig. 6. As can be seen in the two upper panels in Fig. 6, the two measurements give the same result within the measurement precision.

The measured variation of the output amplitude was used to extract the gain dependence on temperature for the detector module. The nominal operating voltage of the APD corresponds to a gain, $M = 50$ at $\lambda_0 = 420$ nm and a temperature, $T = 25$ °C. The gain dependence on the wavelength for an APD can be expressed as [20]:

$$M = \frac{hc}{\lambda} \times \frac{R}{e\eta}, \tag{2}$$

where h is Planck's constant, c the speed of light and λ the wavelength. R is the responsivity (in A/W), e the electron charge and η the quantum efficiency. The relative variations in the scintillation spectrum for CsI(Tl), the responsivity of the APD used, and the quantum efficiency are given in Fig. 9 in Section 3 (with the average values, in the wavelength range from 350–700 nm, for R, and η, being 17 A/W and 73%, respectively). Using this information together with the expression in Eq. (2), the nominal gain weighted over the scintillation spectrum for CsI(Tl) is $M = 43$ at $T = 25$ °C. In the exponential model the dependence of gain, M, on temperature, T, is described by:

$$\frac{1}{M} \times \frac{dM}{dT} = \kappa. \tag{3}$$

Fitting an exponential to the measurement points in the lower left panel of Fig. 6, which gives the gain as function of temperature, gives $\kappa = -3.9 \pm 0.1\%$/K for the detector module investigated in this test. The corresponding fitted curve is given in red in the figure. This result can be compared to the nominal design value of $\kappa = -4.5\%$/K given by the blue curve in the same figure [15,21].

One may also compare to what extent the measured temperature response deviates from the exponential model. When the data is compared to the fit, the residuals report a non-linear behaviour which increases with temperature. Our measurements indicate that the deviation reaches ~1%/K above ~25°C. One possible explanation could be
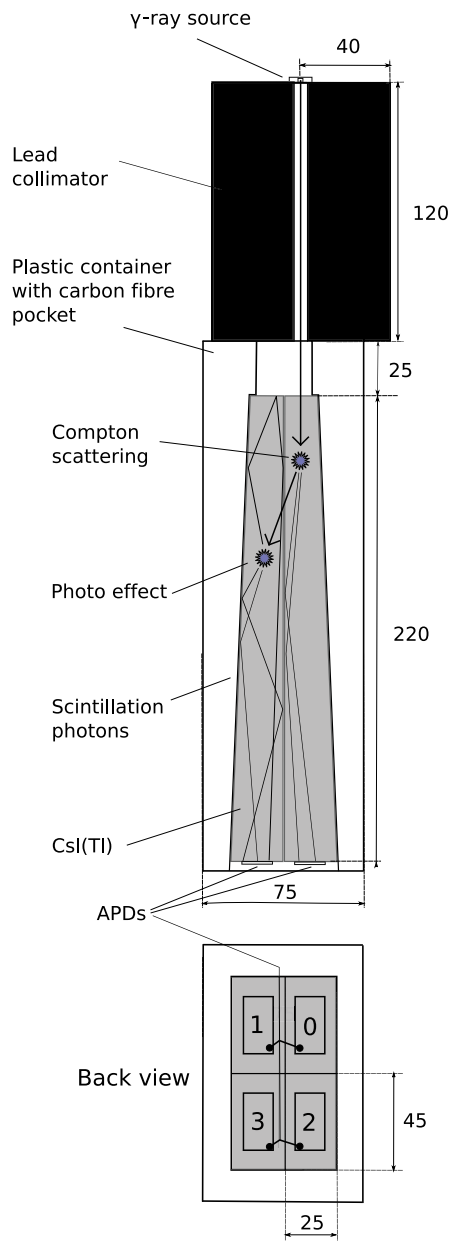
Fig. 7. Overview of the energy add back and light crosstalk measurements. A collimated ^{137}Cs source was placed on top of a 120 mm long collimator centred on the crystal in position 0 of the four crystals fitted into a CALIFA carbon fibre pocket. For the light crosstalk measurements a wrapped plexiglas dummy detector was put in position 1. The distances are given in mm. See text for further details.

Fig. 8. Results of the add back and light crosstalk measurements. The top two rows show coincidence matrices between the indicated crystals when crystal 0 is irradiated by the collimated source, with E0, E1, E2 and E3 being the respective detected amplitudes, calibrated in keV. The notation for the coincidences between crystals follows the numbering scheme in Fig. 7. The 662 keV γ-ray from the ^{137}Cs source, and the 1461 keV background line from ^{40}K [27] are indicated by black dashed lines. In the centre right panel the crystal in position 1 was exchanged by an ESR wrapped plexiglas dummy coupled to an APD. The panels in the last row show the effect of add back when all four positions are filled with CsI(Tl) crystals, together with the effect of different energy thresholds. The red histogram in the lower left panel gives the add back spectrum at 50 keV threshold, while the black spectrum results when no add back is applied. The insert in this panel shows the add back contribution for different applied thresholds. The lower right panel shows the contribution to the add back for different combinations of two crystals. See text for further details. (For interpretation of the references to colour in this figure legend, the reader is referred to the web version of this article.)

due to variations in light yield of the scintillator with temperature. Such an effect has been reported earlier in the literature [25,26], but with somewhat different results. It suffices to say in this work that under realistic conditions the observed gain variation is dominated by changes in APD gain, but that deviations are observed for the detector modules that include the crystal and the APD.

Finally, a gain stability test was also performed in order to evaluate to what extent the temperature compensation in the preamplifier works within the temperature range discussed above. For this measurement the temperature gain stabilization of the preamplifier was activated and the temperature was changed continuously from 25 °C to 22 °C over a time span of ~600 s. The same set of sources as listed above was used. The results are presented in the lower right panel of Fig. 6. It is clear that the temperature compensation produces a comparatively
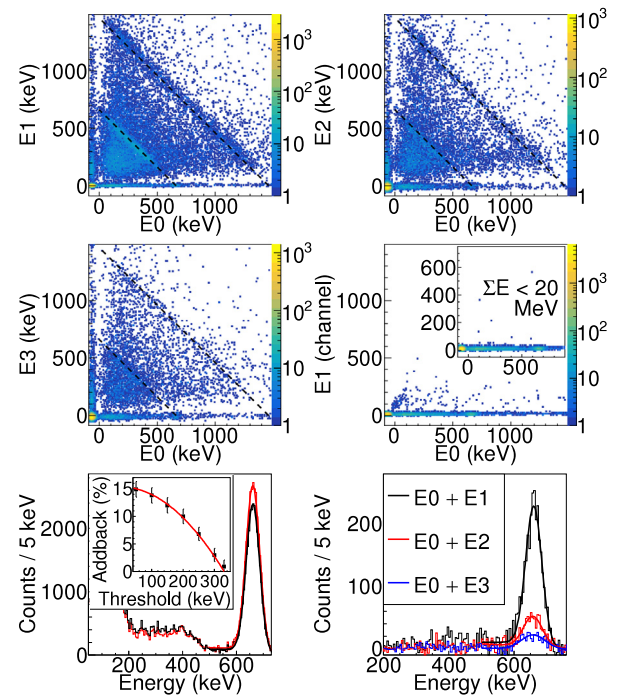
constant output amplitude in the temperature range of interest. For the 662 keV γ-ray line the resolution is 10.5% with the temperature compensation switched off and 8.9% when it is on. For the 1173 keV line the corresponding values are 10.1% without and 6.4% with temperature compensation activated.

Although the results of this test show that the applied temperature compensation produces the expected result at typical operation temperatures, fluctuations observed at higher temperatures require further study. One can conclude however, that at ambient temperatures of ~23 °C used for the resolution and non-uniformity measurements here, the temperature compensation algorithm maintains a constant output amplitude.

2.4. Energy add back and scintillation light crosstalk

For detection of γ-rays in CALIFA, particularly with energies above ~300 keV, energy add back, i.e. summing the signals from several detector elements, due to Compton scattering of γ-rays between elements, becomes important for the total γ-ray detection efficiency. Above the energy threshold for pair production electron–positron annihilation also requires high detection efficiency at energies of a few hundred keV in order to recover the energy that otherwise is lost in single and double escape events. In order to investigate the add back performance, and potential influence of light crosstalk in this energy region, we carried out a series of measurements on the smallest cluster of detectors in

CALIFA, consisting of four detectors placed in a carbon fibre pocket used in the inner mechanical structure. One of detectors was irradiated by a collimated ^{137}Cs source ($E_\gamma = 662$ keV) and the signals from the four detectors were registered in coincidence. The length of the crystals was 22 cm. A sketch of the setup, indicating the irradiated crystal in position 0 and its neighbours, is shown in Fig. 7. The resulting spectra are given in Fig. 8.

In total the add back procedure within the four-crystal cluster, at the minimum threshold of 50 keV, increases the photopeak area by 14.9 ± 1.4%. For multiplicity-two events only, this number is 13.2 ± 0.5%. As expected, among these the largest contribution comes from add back between crystals that share the largest surface area, which contributes 9.4 ± 0.4%. This is followed by add back between crystal 0 and crystal 2 (see Fig. 7) at 2.4 ± 0.3%, and 1.4 ± 0.2% between crystal 0 and 3, respectively. From this measurement, including the small contribution from higher multiplicity events, one can conclude that an add back algorithm using all eight nearest neighbours would increase the number of detected photopeak events by 29.6 ± 2.0%. The resolution of the 662 keV γ-ray in the add-back spectrum changes only by 0.1%, while the centroid is the in the same position, compared to the singles spectrum. The background from ^{40}K is visible in Fig. 8 and add back can also be performed on this γ-ray, even though the crystal for the primary scattering is not determined. Although the two numbers are not directly comparable, it is worth noting that, performing add back on this γ-ray, increases the photopeak area by 63.8 ± 2.2%, compared to the 14.9 ± 1.4% mentioned above. Similar conclusions can be drawn concerning the crystal combinations that give the most important contributions.

An important point to consider for the add back is also the sensitivity to noise and therefore to the threshold that is imposed on individual detector channels. The inset in Fig. 8 shows the add-back efficiency for the 662 keV γ-ray as a function of the threshold level in keV. One can note that the add back contribution to the total photopeak is reduced to 7% at a threshold of 240 keV compared to the 14.9 ± 1.4% for a threshold of 50 keV.

In a second set of measurements, the crystal in position 1 in Fig. 7 was replaced by an ESR-foil wrapped plexiglass dummy coupled to an APD for light crosstalk measurement to estimate the amount of add-back events that do not arise from Compton scattering. The result of this measurement is presented in the centre right panel in Fig. 8, where the coincidence matrices can be compared to the light crosstalk matrix. The positively correlated events in the energy region between 0–300 keV, detected in the dummy, have a hit multiplicity of 3 or 4 and a total energy $\gtrsim 20$ MeV. These events can be attributed to cosmic radiation. The total amount of events detected by the dummy, if cosmic events are included, amounts to 0.3% of the total events detected with an active crystal in position 1. With a cut on energy, to avoid cosmic background, the light cross talk is one order of magnitude smaller, at <0.03%. Consequently, the add back procedure can be performed with a very limited probability for addition of events that are not caused by Compton scattering. This is advantageous as it means that the apertures, given by the granularity of the detector system, that can be used for Doppler correction is not influenced by light cross talk between adjacent modules.

3. Optical and surface properties

A systematic understanding of the interplay of the focussing and absorption effects and their influence on the attainable resolution requires simulations of the light collection process. To perform such simulations, with a result that can be compared to experiments, it is necessary to know several detector-related parameters. As discussed above these include the absorption length of the scintillation light in the CsI(Tl) crystals used, and the reflection properties of the crystal–reflector interface. As part of the development work of the detector, and to facilitate further study, we have performed a series of measurements to deduce these properties for the crystals used in CALIFA. The aim is to use them in a systematic investigation of the light collection in the detector modules. That work is in progress and will be presented later.
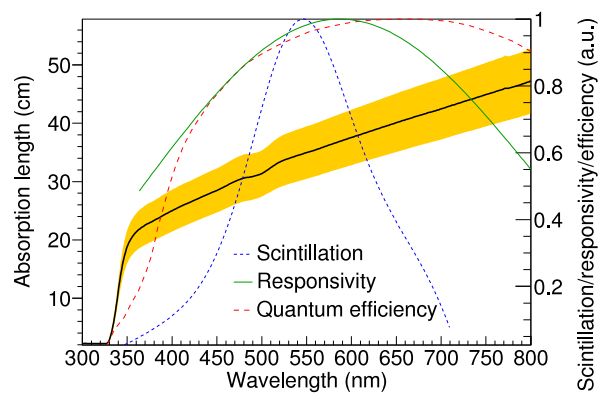

Fig. 9. Results for the absorption length measurements using the spectrophotometer technique. Also indicated in the figure are the CsI(Tl) scintillation spectrum (blue dashed line) [28] and the quantum efficiency and responsivity of the APDs (red dashed and green solid lines, respectively) [21]. See the text for further details. (For interpretation of the references to colour in this figure legend, the reader is referred to the web version of this article.)

3.1. Absorption length and spectrophotometry

Data for the absorption length of CsI(Tl) exist in the literature [29] but studies that cover the full spectral range of the scintillation light in a larger set of crystals made for an actual detector are scarce. For a large set one can expect that variations in the manufacturing process could lead to differences in the absorption length over the crystal sample [11]. For this reason, and to get information about potential spread in the attenuation, we performed measurements on ten detector modules made for CALIFA using a spectrophotometer.[13] It should be noted that the measurements of the attenuation length performed here include all processes that lead to photons not reaching the readout sensor at the end of the crystal.

The spectrophotometer uses two beams of light. One is used for sampling and one as a reference. The attenuation, A, of the light through the crystal is defined as:

$$A = -\log \frac{I}{I_0}, \tag{4}$$

where I is the intensity of the beam after the sample, and I_0 is intensity of the reference beam. The spectral range was set to 300 nm–800 nm with a step of 1 nm. This region covers the CsI(Tl) emission peak between 350 nm and 750 nm, and a significant part of the APD sensitive range 200–1100 nm, as is shown in Fig. 9, where also the sensitivity of the APD as a function of λ is represented, both by the quantum efficiency and the responsivity. The reflection at the entrance and exit surfaces was estimated using the Fresnel equations for perpendicular incidence:

$$R(\lambda) = \left(\frac{n_1(\lambda) - n_2(\lambda)}{n_1(\lambda) + n_2(\lambda)} \right)^2, \tag{5}$$

where $n_1(\lambda)$ is the refractive index of air, and $n_2(\lambda)$ is the refractive index of the crystal. The dependence of the refractive index of air on the wavelength, λ, was neglected and set to be constant, $n_1 = 1$. The refractive index of the crystal, $n_2(\lambda)$, was approximated by a series expansion for undoped CsI:

$$n(\lambda) = \left(a_0 + \lambda^2 \sum_{i=1}^{8} \frac{a_i}{\lambda^2 - b_i^2} \right)^{1/2}, \tag{6}$$

where the parameterization in a_i and b_i are given in Ref. [30]. Under the assumption that the absorption follows a standard Beer–Lambert

---

[13] PerkinElmer LAMBDA 1050UV/Vis.
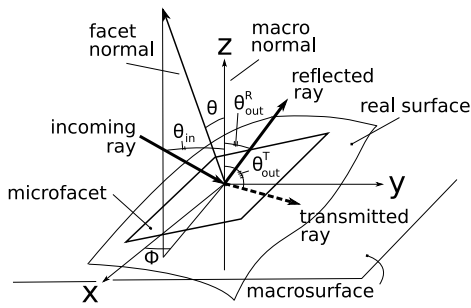
Fig. 10. Detailed view of the microfacet model with an incoming light ray at an angle, θ_{in}, either reflecting at an angle, θ_{out}^R, and remaining inside the crystal, or being transmitted through the surface at an angle, θ_{out}^T, where all angles are given with respect to the indicated z-direction. The macroscopic surface is defined as the average completely flat surface of the crystal, with its normal in the z-direction, and the xy-plane coinciding with the surface. The direction of the microfacet normal is given by the polar angle, θ, and the azimuthal angle, Φ, in this coordinate system. Microfacets whose centre point does not coincide with the plane are situated at a height given by the z-coordinate.

law [31] the absorption length was extracted from the attenuation, taking reflection on the entrance and exit surfaces into account, and neglecting multiple reflections, as:

$$\lambda_L = \frac{L/\ln 10}{A + 2\log(1 - R(\lambda))}, \tag{7}$$

where, λ_L is the absorption length, L the length of the crystal and A and R are defined above. The size of the spectrophotometer sample compartment restricted the maximum length of the crystals to 18 cm. Measurements were done with bare crystals as well as with crystals wrapped in an ESR foil, except at the entrance and exit surfaces. No difference was noticed between the results of these measurements.

The results are shown in Fig. 9. The black central line represents the average absorption length of the ten samples and the coloured area represents the 1σ deviation from the average. Within the spectral range of the CsI(Tl) emission the absorption length varies between ~20 cm and ~40 cm. Weighted over the emission spectrum, the average absorption length from these measurements are 34.6 ± 4.5 cm, which e.g. can be compared to the literature value 39.3 cm in Ref. [29].

The transparency of the ESR foils was measured with the same technique in the wavelength range from 300 nm to 860 nm. The transmission in per cent, weighted over the emission spectrum in the same manner, was 0.26% (and ~0.48% as an unweighted average over the same range). This value is compatible with the <0.03% from the cross talk measurement, taking into account that the crystals are separated by two layers of ESR foil, and that the light falls onto the foil at many different angles in the cross talk measurement, but at ~90° in the transmission measurement.

3.2. Surface topography and atomic force microscopy

Models for simulating light reflection on crystal boundaries, in state-of-the-art detector simulation frameworks, such as GEANT4 [32–34], have typically relied on a subdivision of the macroscopic surface into microfacets whose normals are assumed to have a Gaussian distribution around the direction of the normal of the macroscopic surface (see Fig. 10). Detailed information about this distribution is rarely available for a user of the simulation framework since it will depend not only on the physical nature of the crystal, i.e. the type of scintillator used, but also on the surface treatment applied in each specific case. In addition, models used in such simulations are built on a superposition of specular spike, specular lobe, back scatter spike and Lambertian reflection components. However, it has been shown that not all combinations of scintillator and reflector can be well described in this way [35].

In order to obtain information relevant for the CsI(Tl) detector modules for CALIFA we have used two crystal samples from the same source as for the calorimeter elements and investigated their surface topography. In the following the two samples are denoted as polished and roughed, where this classification should be understood in a relative sense. The aim of this characterization is to provide lookup tables for the surface–reflector interface for CALIFA, and to provide information that can be used in future developments of the calorimeter as well as in other similar projects.

Measurement of the reflection properties at the crystal boundary can be done in several ways. On the one hand one can use a dedicated instrument and specially manufactured crystal samples [35–37]. Such studies have been carried on BGO crystals in the form of half spheres using a laser beam and a movable photodetector. A similar method has also been used to study the surface roughness of flat CsI(Tl) crystals using various surface abrasives [38].

An alternative way, that has been further developed recently, is to measure the surface topography and to simulate the reflection at the interface using the Fresnel equations and ray tracing. Early attempts using this technique were done using profilometers to acquire the statistical distribution of the normals of the microfacets [9]. More recently work has also been done, e.g. for LSO crystals [39,40], using atomic force microscopy.

In this work we performed measurements on CsI(Tl) using an atomic force microscope.[14] A 100×100 μm² surface was scanned, with 100 nm resolution, on two crystal samples: one which was delivered with a polished surface from the manufacturer, and one where we applied a typical lapping procedure using a P400 abrasive[15] in the laboratory. The grid points from the two measurements were used to create triangle tessellated surfaces for which the direction of the microfacet normals were calculated, with θ being the polar angle with respect to the normal of the macroscopic surface and ϕ the azimuthal angle in the plane (see Fig. 10).

The result of the AFM measurement is shown in Fig. 11 where the two upper panels show the surface heights at each grid point measured with respect to a plane fitted to each surface. The two central panels in the same figure give the respective height distributions. One observes, as expected, that the roughed surface exhibits clear troughs and ridges and also has a broader distribution of surface heights. The polished crystal in this example also has a rather varied surface structure and both samples show clear signs of surface treatment leading to preferred directions of the structural variations in the surface.

Typical parameters used to quantify surface roughness include the root-mean-square (RMS) of the surface height and slope distributions. Here we refer to Ref. [9] for further details concerning the definitions of both these quantities and their use in other work. In the current study the height above the fitted plane, that defines the zero level as mentioned above, is denoted by z_i. The mean height, $\bar{z}$, over the zero level plane is thus given by:

$$\bar{z} = \frac{1}{N}\sum_{i=1}^{N} z_i, \tag{8}$$

where N is the number of measurement points. For the RMS of the surface heights, z_i, we give this value with respect to the mean height, $\bar{z}$, i.e. as the standard deviation, σ_z, of the height distribution:
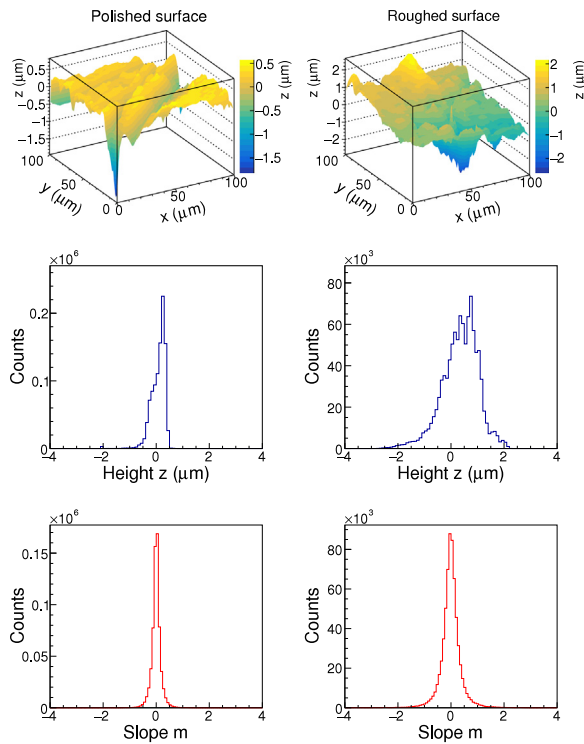
$$\sigma_z = \sqrt{\frac{1}{N}\sum_{i=1}^{N}(z_i - \bar{z})^2}, \tag{9}$$

where all terms are defined as above. Similarly, the slope in the i:th measurement point, m_i, is defined as:

$$m_i = \frac{z_{i+1} - z_i}{\tau_0}, \tag{10}$$

---

[14] Bruker GmbH Nanowizard.
[15] Mirka Ltd.

Fig. 11. Results from atomic force microscopy for a polished (left column) and roughed (right column) CsI(Tl) sample. The two upper panels show the two CsI(Tl) crystal surfaces measured with atomic force microscopy (AFM). The two central panels show the distribution of heights, z, for the two surfaces, measured from the height given by a plane fitted to the respective surface. The two lower panels show the distribution of slopes, m, for the two surfaces. See text for further details.

where τ_0 is the step length, i.e. 100 nm, in this work. The mean slope, $\overline{m}$, and the standard deviation of the slope distribution, σ_m, are given in the same manner as for the mean height:

$$\overline{m} = \frac{1}{N_s} \sum_{i=1}^{N_s} m_i \quad \text{and} \quad \sigma_m = \sqrt{\frac{1}{N_s} \sum_{i=1}^{N_s} (m_i - \overline{m})^2}, \quad (11)$$

where N_s is the number of measurement points for the slope distribution. Slope distributions for the two samples are given in the two lower panels in Fig. 11.

For the two surfaces investigated here the parameters introduced above were calculated to be $\overline{z} = 78$ nm and $\overline{m} = -0.001$ for the polished surface, and $\overline{z} = 345$ nm and $\overline{m} = -0.012$, for the roughed surface, with the slopes calculated in the x-direction. The variation in these distributions was calculated to be $\sigma_z = 273$ nm and $\sigma_m = 0.195$ for the polished surface. For the roughed surface the corresponding values were found to be $\sigma_z = 689$ nm and $\sigma_m = 0.433$. See Fig. 11 for the respective histograms.

The slopes were also calculated in the y-direction which gave $\overline{m} = 0.002$ and $\sigma_m = 0.168$, for the polished surface, and $\overline{m} = 0.015$ and $\sigma_m = 0.224$ for the roughed surface. Due to the directions observed in the two surfaces, it is not surprising that these slope distributions vary depending on direction, and due to its rather roughed character, that the polished surface has a similar variation in the slope distribution as the roughed surface in one direction. The estimated errors are ±10 nm over the full surface. How the microfacets relate to the macroscopic surface is illustrated in Fig. 10.

It is interesting to compare these results with the early work reported in Ref. [9]. In that study it was speculated that the relatively small values that were extracted for the RMS slope for the roughed surfaces investigated there, could be attributed to the relatively low resolution of the profilometer. Simulations and comparisons to light output non-uniformity for the long tapered roughed BGO crystals in that work made the authors propose that the RMS slope of the roughed surfaces involved should be significantly larger than the RMS slopes of ~0.1 that were measured, and be closer to ~0.7–1 to reproduce observations. The results of that work also pointed towards the investigated polished surface having an RMS slope noticeably different from zero. The assumptions concerning the RMS slope in that work are largely confirmed in this study. This can be an indication that the current results can be useful for further simulations of light output non-uniformity in CsI(Tl) crystals.

In addition to the surface roughness parameters discussed above one can also investigate the θ distribution of the microfacet normals (see the two upper panels of Fig. 12). It is clear that the maximum in the respective distribution is shifted from zero, which would be the dominant polar angle for a perfectly flat specular reflector, due to the existence of troughs and ridges with a specific direction over the surface. The average normal for each surface does, however, only deviate 0.05° for the polished surface, and 0.18° for the roughed surface, from the macro surface normal. For the polished case at least two superimposed distributions can be seen, one with a maximum at ~2° and one at ~15°. Selections of subranges over the surface also confirm that the distribution consists of several sub-distributions. The conclusion is the same for the roughed surface where several microfacet distributions create an almost flat top distribution of θ angles as can be seen in the top right panel of the same figure. One should note here that the two distributions given in the two top panels in Fig. 12 are not normalized over the solid angle and do therefore not give the density of normals in a specific direction. For the two distributions in the central panels such a normalization has been made. One can conclude, however, that neither the distributions in the two top panels, nor the normalized distributions in the two central panels, have Gaussian shape.

A program was also written to perform a ray tracing simulation over the microfacets to calculate the reflection and transmission angles with respect to the macro surface for given pairs of incoming angles, θ_i and ϕ_i. The program functions so that a random point is selected on the surface and the direction of the microfacet normal is calculated. A photon is then created, with a wavelength determined by the probability distribution defined by the scintillation spectrum. The photon is simulated to impinge onto the surface in a random direction while ensuring that it falls onto the microfacet from the inside of the crystal. The transmission and reflection probabilities are then calculated for the incoming angle with respect to the microfacet normal using the Fresnel equations and Snell's law for the given wavelength.

As an example, the difference between the incoming and reflection angles with respect to the macroscopic surface is presented in the two lower panels of Fig. 12. For the case of specular reflection from a flat surface one would expect a point-like distribution in the centre of the presented two-dimensional histograms. The simulation shows the expected behaviour with a widening of the distributions, as well the introduction of a deviation from complete symmetry due to the use of a real surface. Furthermore, the widening observed in the θ distribution dominates while relatively narrow bands extend over the full angular range along the direction of the ϕ axis. One can conclude that the broadening of the distribution is directly correlated to the wider θ distribution observed for the roughed surface compared to the polished one. The weak narrow bands that extend over the full range in the ϕ direction can be explained by relatively flat sections of the crystal, where the microfacet normals can point in any ϕ direction. The aim is to use the measured distributions to create lookup tables for simulations of the light collection in the CALIFA detector modules. One may from such simulations be able to predict the influence on the light output non-uniformity, that is the dominating effect for variations in the attained resolution in this work, in order to see if detailed preferred strategies for lapping can be identified. That work is in progress.
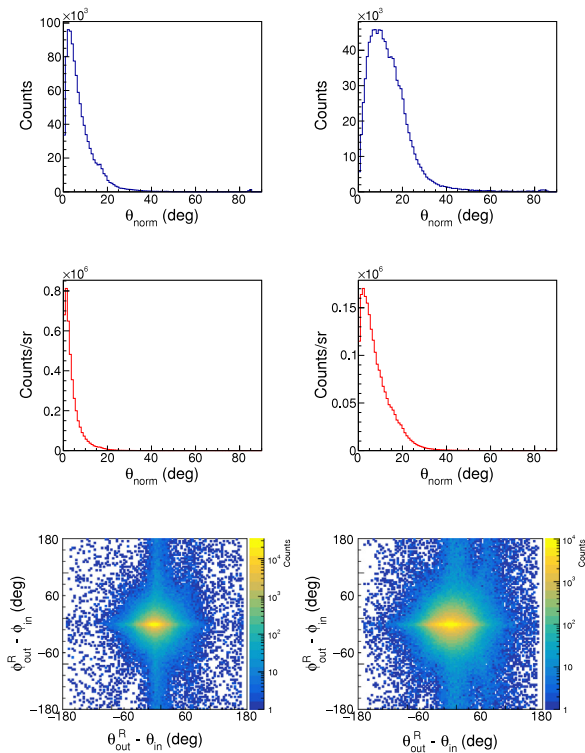
Fig. 12. Results for the polished (left column) and roughed surfaces (right column) shown in the two top panels of Fig. 11. The two top panels show the polar angle distributions for the microfacet normals. The same distributions normalized to the solid angle are given in the two central panels. The deviation from specular reflection for a light ray falling onto the respective surfaces at incoming angles θ_{in} and Φ_{in}, and reflecting into angles θ_{out}^R and Φ_{out}^R is shown in the two lower panels. See text for further details.

4. Summary and conclusion

A set of 478 detector modules for the calorimeter, CALIFA, developed for the R^{3}B experiment at FAIR, has been investigated as to resolution, light output non-uniformity, relative efficiency and total light output. The results show that for crystals of the geometry needed for a calorimeter of this kind, the main source of variations in resolution can be attributed to light output non-uniformity arising from the interplay of absorption of scintillation photons in the medium, and the focussing effect caused by the geometry. The attained average resolution for the investigated sample, which has undergone surface lapping for minimization of this effect, is 5.2% at 1275 keV. However, the observed correlation between resolution and light output non-uniformity indicates that the best attainable resolution would be 4.4% if the dependence on light output non-uniformity is eliminated. Measurements of the noise originating in the readout chain were also carried out, to quantify its contribution to detector performance, and was found to add less than 0.1% to the resolution. In addition the APD gain stabilization with respect to temperature was examined and it was found that with applied stabilization gain variations are negligible within the relevant temperature region.

A cluster of 4 crystals was irradiated with a γ-ray source for energy add back and crosstalk measurements. A maximum gain of ~30% in the peak intensity for 662-keV γ-rays was derived for a crystal surrounded by others in all directions with negligible losses in energy accuracy and precision. The crosstalk probability between neighbouring crystals was less than 3×10^{-4}, demonstrating the light tightness of the ESR foils.

Parameters of importance for simulation of light collection in CsI(Tl) scintillation crystals were also determined. The absorption length was measured using spectrophotometry, in the wavelength region between 300 and 800 nm, for a sample of 10 crystals, and was found to be 34.6 ± 4.5 cm if weighted over the scintillation spectrum. Finally, for future simulation work the surface topography was investigated using atomic force microscopy and it was concluded that the distribution of surface normals consists of a combination of sub-distributions, featuring troughs and ridges in the crystal surface, and that these sub-distributions creates deviations from the standard Gaussian model typically used in state-of-the art simulation frameworks.

Acknowledgements

References

[1] O. Tengblad, NUSTAR and the status of the R^{3}B project at FAIR, Pramana 75 (2010) 355–361.

[2] M. Durante, et al., All the fun of the FAIR: fundamental physics at the facility for antiproton and ion research, Phys. Scr. 94 (3) (2019) 033001.

[3] D. Cortina-Gil, et al., CALIFA, a dedicated calorimeter for the R^{3}B/FAIR, Nuclear Data Sheets 120 (SI) (2014) 99–101.

[4] H. Alvarez Pol, et al., Performance analysis for the CALIFA barrel calorimeter of the R3B experiment, Nucl. Instrum. Methods. Phys. Res. A 767 (2014) 453–466.

[5] M. Winkel, Dissertation Dr. Rer. Nat Komplexe Pulsformalgorithmen Und Teilchenidentifikation Zur Echtzeit-IMplementierung in CALIFA, Fakultät für Physik Technischen Universität München, 2016.

[6] O. Tengblad, et al., LaBr3(Ce):LaCl3(Ce) Phoswich with pulse shape analysis for high energy gamma-ray and proton identification, Nucl. Instrum. Methods Phys. Res. A 704 (2013) 19–26.

[7] E. Auffray, et al., Crystal conditioning for high-energy physics detectors, Nucl. Instrum. Methods Phys. Res. A 486 (2002) 22–34.

[8] S. Diehl, et al., Impact of non-uniformity in light collection on the energy resolution of the PANDA electromagnetic calorimeter at photon energies below 1 GeV, J. Phys. Conf. Ser. 928 (2017) 012040.

[9] J. Bea, A. Gadea, L.M. Garcia-Raffi, J. Rico, B. Rubio, J.L. Tain, Simulation of light collection in scintillators with rough surfaces, Nucl. Instrum. Method Phys. Res. A 350 (1994) 184–191.

[10] J.B. Birks, The Theory and Practice of Scintillation Counting, Pergamon Press, 1964.

[11] L. Trefilova, B. Grinyov, V. Alekseev, A. Mitichkin, V.Y. Yakovlev, A. Meleshko, Photo- and radiation-stimulated processes in CsI(Tl) crystals, IEEE Trans. Nucl. Sci. 55 (3) (2008) 1263–1269.

[12] A. Gektin, B. Grinyov, D.I. Zosim, A. Boyarintsev, Light output tuning for the long-length CsI(Tl) scintillators, Nucl. Instrum. Methods Phys. Res. A 598 (2009) 270–272.

[13] N. Grassi, G. Casini, M. Frosini, G. Tobia, T. Marchi, Pixe characterization of CsI(Tl) scintillators used for particle detection in nuclear reactions, Nucl. Instrum. Methods Phys. Res. B 266 (2008) 2383–2386.

[14] P. Yang, C.D. Harmon, F.P. Doty, J.A. Ohlhausen, Effect of humidity on scintillation performance in Na and Tl activated CsI crystals, IEEE Trans. Nucl. Sci. 61 (2) (2014) 1024–1031.

[15] D. Cortina-Gil, et al., Technical Report for the Design, Construction and Commissioning of the CALIFA Barrel: The R^{3}B CALorimeter for In Flight detection of γ-rays and high energy charged pArticles. URL https://edms.cern.ch/document/1833500/1.

[16] H.G. Essel, et al., The new data acquisition system at gsi, IEEE Trans. Nucl. Sci. 43 (1) (1996) 132.

[17] H.G. Essel, N. Kurz, The general purpose data acquisition system mbs, IEEE Trans. Nucl. Sci. 47 (2) (2000) 337–339.

[18] E. Browne, J.K. Tuli, Nuclear data sheets for A=137, Nucl. Data Sheets 108 (2007) 2173.

[19] M.S. Basunia, Nuclear data sheets for A = 22, Nucl. Data Sheets 127 (2015) 69.

[20] C.R. Pollock, Fundamentals of Optoelectronics, Richard D. Irwin Inc., 1995.

[21] Hamamtsu Photonics K.K. Solid State Division, Short Wavelength Type APD, Catalogue, 2017.

[22] K. Deiters, et al., Properties of the avalanche photodiodes for the CMS electromagnetic calorimeter, Nucl. Instrum. Methods Phys. Res. A 453 (2000) 223.

[23] A. Vandenbroucke, T.J. McLaughlin, C.S. Levin, Influence of temperature and bias voltage on the performance of a high resolution PET detector built with position sensitive avalanche photodiodes, J. Instrum. 7 (08) (2012) P08001.

[24] P. Mars, Temperature dependence of avalanche breakdown voltage in p—n junctions, Intern. J. Elect. 32 (1) (1972) 23–37.

[25] R. Mao, L. Zhang, R. Zhu, Optical and scintillation properties of inorganic scintillators in high energy physics, IEEE Trans. Nucl. Sci. 55 (4) (2008) 2425–2431.

[26] J. Valentine, W.W. Moses, S. Derenzo, D.K. Wehe, G.F. Knoll, Temperature dependence of csi(tl) gamma-ray excited scintillation characteristics, Nucl. Instrum. Methods Phys. Res. A 325 (1993) 147–157.

[27] J. Chen, Nuclear data sheets for A=40, Nucl. Data Sheets 140 (2017) 1.

[28] Saint-Gobain Ceramics and Plastics, Inc., CsI(Tl), CsI(Na) Cesium Iodide Scintillation Material, Catalogue, 2017.

[29] M. Tanabashi, et al., Review of particle physics, Phys. Rev. D 90 (2018) 467.

[30] H.H. Li, Refractive index of alkaline earth halides and its wavelength and temperature derivatives, J. Phys. Chem. Ref. 9 (1980) 161–290.

[31] S. Svanberg, Atomic and Molecular Spectroscopy, Basic Aspects and Practical Applications, Springer-Verlag, 2001.

[32] S. Agostinelli, et al., Geant4 - a simulation toolkit, Nucl. Instrum. Methods Phys. Res. A 506 (3) (2003) 250–303.

[33] J. Allison, et al., Geant4 developments and applications, IEEE Trans. Nucl. Sci. 53 (1) (2006) 270–278.

[34] J. Allison, et al., Recent developments in Geant4, Nucl. Instrum. Methods Phys. Res. A 835 (2016) 186–225.

[35] M. Janecek, W.W. Moses, Simulating scintillator light collection using measured optical reflectance, IEEE Trans. Nucl. Sci. 57 (3) (2010) 964–970.

[36] M. Janecek, W.W. Moses, Optical reflectance measurements for commonly used reflectors, IEEE Trans. Nucl. Sci. 55 (2008) 2432–2437.

[37] M. Janecek, W.W. Moses, Measuring light reflectance of bgo crystal surfaces, IEEE Trans. Nucl. Sci. 55 (2008) 2443–2449.

[38] I. Kilimchuk, V. Tarasov, J. Alameda, A.A. Bobovnikov, A. Boyarintsev, S.N. Kovalchuk, Study of surface roughness of CsI:Tl crystals treated by various abrasives, IEEE Trans. in Nucl. Sci. 56 (2009) 2966–2971.

[39] E. Roncali, S. Cherry, Simulation of light transport in scintillators based on 3d characterization of crystal surfaces, Phys. Med. Bio. 58 (2013) 2185–2198.

[40] M. Stockhoff, et al., Advanced optical simulation of scintillation detectors in gate v8.0: first implementation of a reflectance model based on measured data, Phys. Med. Bio. 62 (2017) L1–L8.